ROYAL SOCIETY OF CHEMISTRY

PAPER

Check for updates

Thermodynamically favored stable hydrogen storage reversibility of NaBH$_4$ inside of bimetallic nanoporous carbon nanosheets†

Wei Chen,[a] Shunlong Ju,[a] Yahui Sun,[a] Tianren Zhang,[b] Juan Wang,[b] Jikai Ye,[a] Guanglin Xia [ID] *[a] and Xuebin Yu*[a]

Sodium borohydride (NaBH$_4$) has been widely regarded as a potential hydrogen storage material due to its high gravimetric and volumetric capacity. Its practical application, however, is hindered by the high operating temperature of over 500 °C and extremely poor reversibility. Herein, thermodynamically favored reversible hydrogen storage performance of NaBH$_4$ is developed inside of bimetallic (NiCo) nanoporous carbon nanosheets. Benefiting from the synergetic effect of nanoconfinement and the catalytic role of NiCo alloys, the apparent activation energy for H$_2$ desorption from NaBH$_4$@NiCo-NC is reduced to 36.8 kJ mol^{-1} with the complete H$_2$ desorption at only 400 °C, resulting in the simultaneous formation of NiB and CoB as the dehydrogenation products. More interestingly, the reversible transformation between NiB/CoB and Ni$_2$B/Co$_2$B that are *in situ* formed during the subsequent re-/dehydrogenation process acts as a B reservoir, leading to a significant decrease of Gibbs free energy change for the reversibility of NaBH$_4$ to 1.41 eV, 0.62 eV lower than that of pure NaBH$_4$. As a result, coupled with the catalytic role of *in situ* formed Co$_2$B/Ni$_2$B in promoting the H$_2$ desorption performance of NaBH$_4$, a stable reversible capacity of 9.0 wt% is realized for NaBH$_4$ at a temperature as low as 400 °C for 5 cycles.

Introduction

The world is facing critical environmental and energy issues, and the advancement of clean and environmentally friendly technologies is vital for us to achieve a clean energy future.[1,2] The hydrogen economy, which could satisfy the ever-growing global energy needs while reducing the emission of carbon dioxide and other greenhouse gas emissions, has been widely regarded as an alternative to the traditional energy landscape based on fossil fuels.[3–5] Due to the ultralow density of hydrogen (0.0899 g L^{-1}) at standard temperature and pressure, developing a safe, effective, and economical way to store hydrogen is a necessary step towards the wide application of the hydrogen energy, particularly for on-board energy carrier.[6,7] Therefore, complex hydrides attract intensive attention as hydrogen storage materials due to their high gravimetric and volumetric hydrogen densities.[8–10] As the first known borohydride, NaBH$_4$, possessing a high gravimetric and volumetric density of 10.8 wt% and 115 kg m^{-3}, respectively, is among the most investigated hydrogen storage materials with low toxicity.[11–13]

Unfortunately, the operating temperature for the release of hydrogen from NaBH$_4$ is in general over 500 °C attributed to its high thermodynamic stability and sluggish kinetics.[14,15] More importantly, the reversibility of NaBH$_4$ is highly limited because the phase separation and the evaporation of sodium occurred during the dehydrogenation process.[16,17]

To date, one of the most effective approaches to address the above-mentioned issues is reducing the particle size of NaBH$_4$ to the nanometer range, which could effectively shorten the diffusion pathway of H$_2$ towards reversible hydrogenation and dehydrogenation processes and hence results in the decrease of the operating temperature and fast H$_2$ desorption and adsorption kinetics.[18,19] Unfortunately, upon long-term heating for cycling H$_2$ storage, the particles of NaBH$_4$ with nanometer sizes tend to aggregate and grow to minimize their surface energy, which could inevitably deteriorate the size effect in improving H$_2$ desorption and adsorption performance of NaBH$_4$.[2] Therefore, nanoconfinement of NaBH$_4$ into porous scaffolds has been developed to synthesize and stabilize NaBH$_4$ nanoparticles (NPs) *via* taking advantage of the structural support role of scaffolds to inhibit the sintering and growth of the thus-formed NaBH$_4$ NPs.[20,21] Moreover, the physical confinement role of porous scaffolds is capable of effectively suppressing the evaporation of sodium, which effectively contributes to the enhancement of cycling stability of NaBH$_4$ for hydrogen storage.[20,22] Furthermore, inspired by the important role of

[a]Department of Materials Science, Fudan University, Shanghai 200433, China. E-mail: xiaguanglin@fudan.edu.cn; yuxuebin@fudan.edu.cn

[b]Zhejiang Tianneng Battery Co., Ltd., Changxing 313100, Zhejiang, China

† Electronic supplementary information (ESI) available. See DOI: 10.1039/d1ta10361j

7122 | *J. Mater. Chem. A*, 2022, **10**, 7122–7129

This journal is © The Royal Society of Chemistry 2022

catalysts in enhancing the H_2 desorption and adsorption of $NaBH_4$, the combination of nanoconfinement and catalysts has been realized *via* using functional scaffolds that have catalytic effect in improving the hydrogen storage performance of $NaBH_4$ or decorating $NaBH_4$ with catalysts to further promote the hydrogen storage performance of $NaBH_4$.[23–27] Although the synergistic effect of nanoconfinement and catalysts plays an important role in improving the reversibility of $NaBH_4$ to a large extent, the lack of control over tuning the thermodynamic stability of $NaBH_4$ results in the limited cycling stability under moderate conditions for on-board hydrogen storage.[16,28–30]

Herein, we develop a thermodynamically favored reversible hydrogen storage process of $NaBH_4$ inside of bimetallic (NiCo) nanoporous carbon nanosheets (denoted as NiCo-NC) derived from the carbonization of NiCo-MOF nanosheets. As schematically illustrated in Fig. 1a, the nanoconfinement of $NaBH_4$ into NiCo-NC not only results in the uniform formation of $NaBH_4$ NPs, but also promotes the thermodynamic destabilization reaction between $NaBH_4$ and NiCo alloy NPs that are homogeneously distributed inside of NiCo-NC. This thermodynamically

and kinetically improves the initial dehydrogenation process of $NaBH_4$ with the formation of NiB and CoB as the dehydrogenation products. Benefiting from this unique structure, a complete dehydrogenation of $NaBH_4$ could be realized at a temperature as low as 440 °C. More importantly, upon the subsequent hydrogen storage process, a thermodynamically favored reversible hydrogen storage process of $NaBH_4$ is observed based on the reversible transformation between NiB/CoB and Ni_2B/Co_2B. Induced by the reversible transformation between NiB/CoB and Ni_2B/Co_2B, acting as the B reservoir, the Gibbs free energy change for the hydrogen storage of $NaBH_4$ is significantly decreased to 1.41 eV, 0.62 eV lower than that of the bulk counterpart. As a result, a stable reversible hydrogen storage capacity of 9.0 wt% is achieved for $NaBH_4$ at 400 °C for five cycles.

Results and discussion

As illustrated in Fig. 1a, the nanoconfinement of $NaBH_4$ into the NiCo-NC template is realized through a facile solution
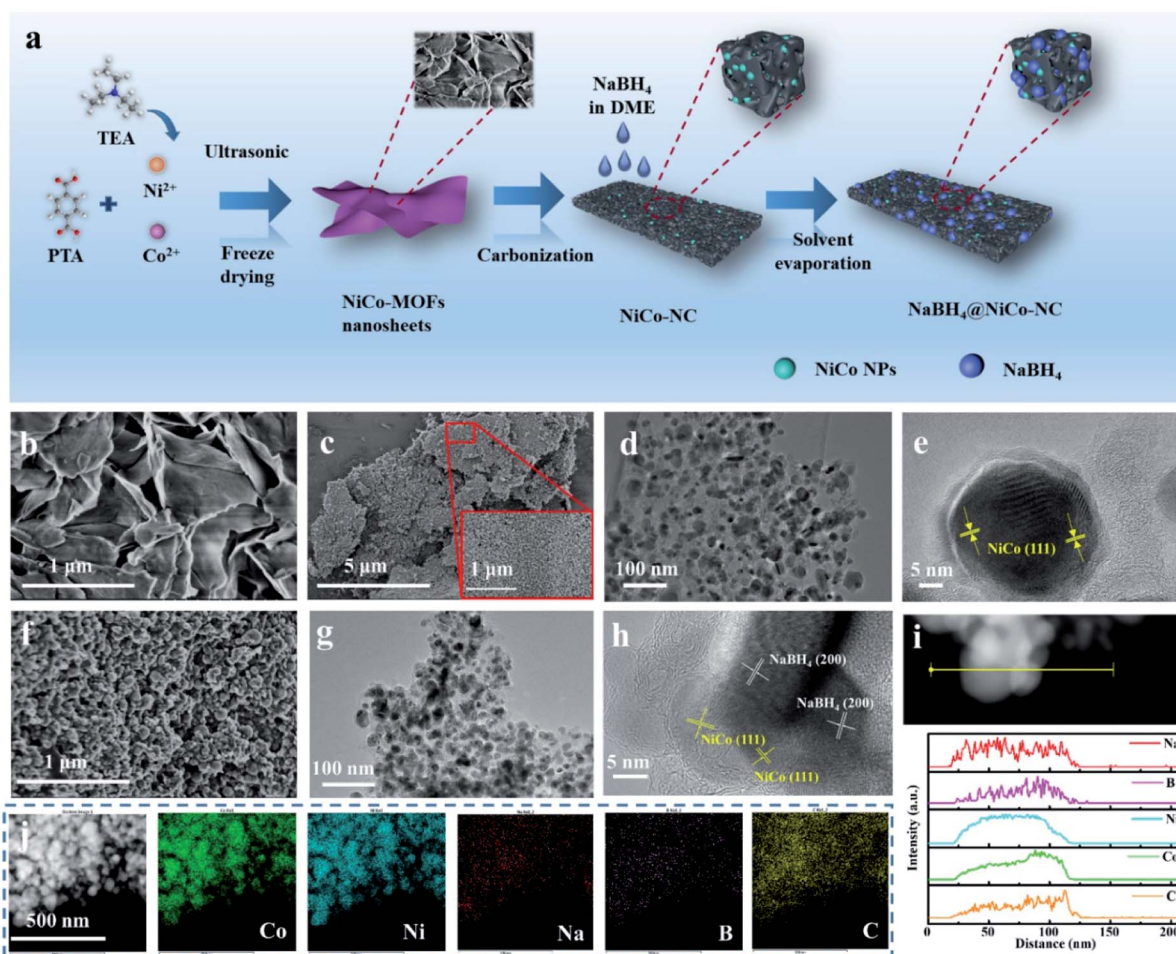

Fig. 1 (a) Schematic diagram of the synthesis procedure of $NaBH_4$@NiCo-NC. SEM images of the as-synthesized (b) NiCo-MOFs and (c) NiCo-NC. (d) TEM and (e) HRTEM images of NiCo-NC. (f) SEM, (g) TEM and (h) HRTEM images of the as-prepared $NaBH_4$@NiCo-NC. (i) TEM image and the corresponding line-scan TEM-EDS elemental distribution curves of N $NaBH_4$@NiCo-NC. (j) STEM image and the relative EDS elemental mapping images of $NaBH_4$@NiCo-NC.

This journal is © The Royal Society of Chemistry 2022

J. Mater. Chem. A, 2022, **10**, 7122–7129 | **7123**

infiltration method. First, 2D NiCo-MOFs that have an ultrathin sheet-like structure as evidenced by scanning electron microscopy (SEM) images are synthesized according to the ultrasonic and freeze-drying method (Fig. 1b). The X-ray diffraction (XRD) results (Fig. S1†) exhibit the characteristic peaks of NiCo-MOFs that are isostructural to the previously reported Ni-based MOFs (no. 985792, space group of $C2/m$), which directly demonstrates the formation of NiCo-MOFs.[31] After the carbonization treatment of the as-synthesized NiCo-MOFs treated by the freeze-drying process, the 2D sheet-like structure is well preserved (Fig. 1c) and the typical diffraction peaks of NiCo alloys could be clearly observed in the XRD patterns of thus-obtained NiCo-NC. SEM images illustrate that the surface of thus-obtained NiCo-NC is composed of a porous structure constructed by the well-distributed NiCo NPs, which provides sufficient spaces for the subsequent infiltration of $NaBH_4$. The uniform distribution of NiCo NPs could be further supported by the transmission electron microcopy (TEM) results, which validate the presence of NiCo NPs with particle sizes ranging from 15 to 30 nm (Fig. 1d). The high-resolution TEM (HRTEM) image (Fig. 1e) exhibits a typical lattice spacing of 0.205 nm that could be indexed to the (111) plane of NiCo alloys, indicating the formation of NiCo alloys, which corresponds well with the XRD results (Fig. S1†). In addition, it could be clearly observed that each NiCo NP is uniformly surrounded by ultrathin carbon layers with a thickness of around 2 nm, which are capable of alleviating the agglomeration and particle growth of NiCo NPs upon thermal heating for reversible hydrogen storage. X-ray photoelectron spectroscopy (XPS) is further employed to analyze the chemical valence states of NiCo in NiCo-NC. Two fitting peaks located at around 778.3 and 793.7 eV in the high-resolution XPS spectrum of Co 2p and two fitting peaks located at around 852.8 and 870.0 eV in the high-resolution XPS spectrum of Ni 2p could be indexed to NiCo alloys (Fig. S2†).[32,33] The presence of high-valence Co and Ni species is probably attributed to partial surface oxidation of metallic Co or Ni during the transfer of samples for XPS measurement.

After the nanoconfinement of $NaBH_4$ into NiCo-NC via the facile solvent-infiltration method, the 2D nanosheet structure of the as-synthesized NiCo-NC is well maintained (Fig. 1f and g). XRD patterns (Fig. S1†) confirm the presence of characteristic peaks of $NaBH_4$ and the FTIR spectrum (Fig. S3†) exhibits the signature absorption peaks of $NaBH_4$ bending at 1119 cm^{-1} and stretching at 2226, 2300, and 2339 cm^{-1}, respectively, indicating the successful infiltration of $NaBH_4$. The HRTEM image (Fig. 1h) illustrates typical lattice planes of $NaBH_4$ and NiCo alloys with intimate contact, in good agreement with the XRD and FTIR results, which provides further evidence for the successful nanoconfinement of $NaBH_4$ into the framework of NiCo-NC. The EDS line-scan elemental distribution profiles (Fig. 1i) over one individual NiCo NP of NiCo-NC illustrate that the distribution of Na and B elements agrees well with that of Ni, Co, and C of NiCo-NC throughout the whole NiCo NPs, which provides additional evidence for the uniform coverage of $NaBH_4$ NPs on the surface of NiCo NPs uniformly distributed inside of NiCo-NC. More importantly, according to the energy-dispersive X-ray spectroscopy (EDS) elemental mapping results

(Fig. 1j), the signals of Na and B of $NaBH_4$ correspond well with those of Ni, Co, and C of NiCo-NC, which directly demonstrates the homogeneous distribution of $NaBH_4$ NPs inside of NiCo-NC.

The H_2 desorption performance of $NaBH_4$@NiCo-NC is first investigated using mass spectrometry (MS) (Fig. 2a). Owing to the sluggish dehydrogenation kinetics, an onset hydrogen desorption temperature as high as 523 °C could be observed for the ball-milled $NaBH_4$ with a peak temperature of 545 °C. It is interesting to note that the onset temperature for the dehydrogenation of $NaBH_4$ could be decreased remarkably to 308 °C after the addition of NiCo-NC via the ball-milling process, demonstrating the excellent catalytic effect of NiCo-NC in improving the hydrogen desorption performance of $NaBH_4$. The major peak temperature for the dehydrogenation of $NaBH_4$/ NiCo-NC, however, is still as high as 468 °C. In strong contrast, after down-sizing into the nanometer scale via nanoconfinement into NiCo-NC, the peak temperature for the dehydrogenation of $NaBH_4$ could be decreased to approximately 356 °C, 112 °C lower than that of the ball-milled counterpart and 189 °C lower than that of bulk $NaBH_4$, indicating the synergistic role of nanoconfinement and catalytic effect of NiCo-NC in effectively improving the H_2 desorption performance of $NaBH_4$. Interestingly, upon nanoconfinement of $NaBH_4$ into NiCo-NC with the complete etching of NiCo alloys (denoted as $NaBH_4$@NC), which still maintains the 2D nanoporous structure of NiCo-NC with the disappearance of NiCo alloys as verified by the XRD results (Fig. S1†), the onset temperature and the peak temperature of $NaBH_4$@NC could also be decreased to 343 °C and 425 °C, respectively. This result directly demonstrates that the decrease of the particle size could enhance the H_2 desorption performance of $NaBH_4$ to a large extent. Both the onset and peak temperature, however, are still much higher than those of $NaBH_4$@NiCo-NC, which provides direct evidence for the catalytic role of NiCo NPs in enhancing the H_2 desorption performance of $NaBH_4$ NPs.

Subsequently, volumetric dehydrogenation values are investigated at various temperatures to evaluate the H_2 desorption kinetics of $NaBH_4$@NiCo-NC. As shown in Fig. 2b, only 1.4 wt% hydrogen could be released from bulk $NaBH_4$ within 6 h at 440 °C due to its high thermodynamic stability and sluggish dehydrogenation kinetics. Owing to the catalytic role of NiCo-NC, the hydrogen desorption capacity of $NaBH_4$/NiCo-NC is remarkably increased to 6.9 wt% even upon decreasing the temperature to 380 °C. By comparison, the hydrogen capacity released from $NaBH_4$@NiCo-NC under identical conditions reaches 8.5 wt%, much higher than that of the ball-milled counterpart, demonstrating the synergistic effect of nanoconfinement and catalytic role of NiCo-NC in enhancing the hydrogen desorption performance of $NaBH_4$. It is interesting to note that upon etching of NiCo NPs from NiCo-NC, only 5.6 wt% hydrogen could be released from the as-prepared $NaBH_4$@NC under identical conditions, which provides additional evidence for the important role of NiCo NPs in improving the H_2 desorption performance of $NaBH_4$. To further explore the influence of NiCo-NC on the dehydrogenation kinetics of $NaBH_4$@NiCo-NC, isothermal dehydrogenation measurements
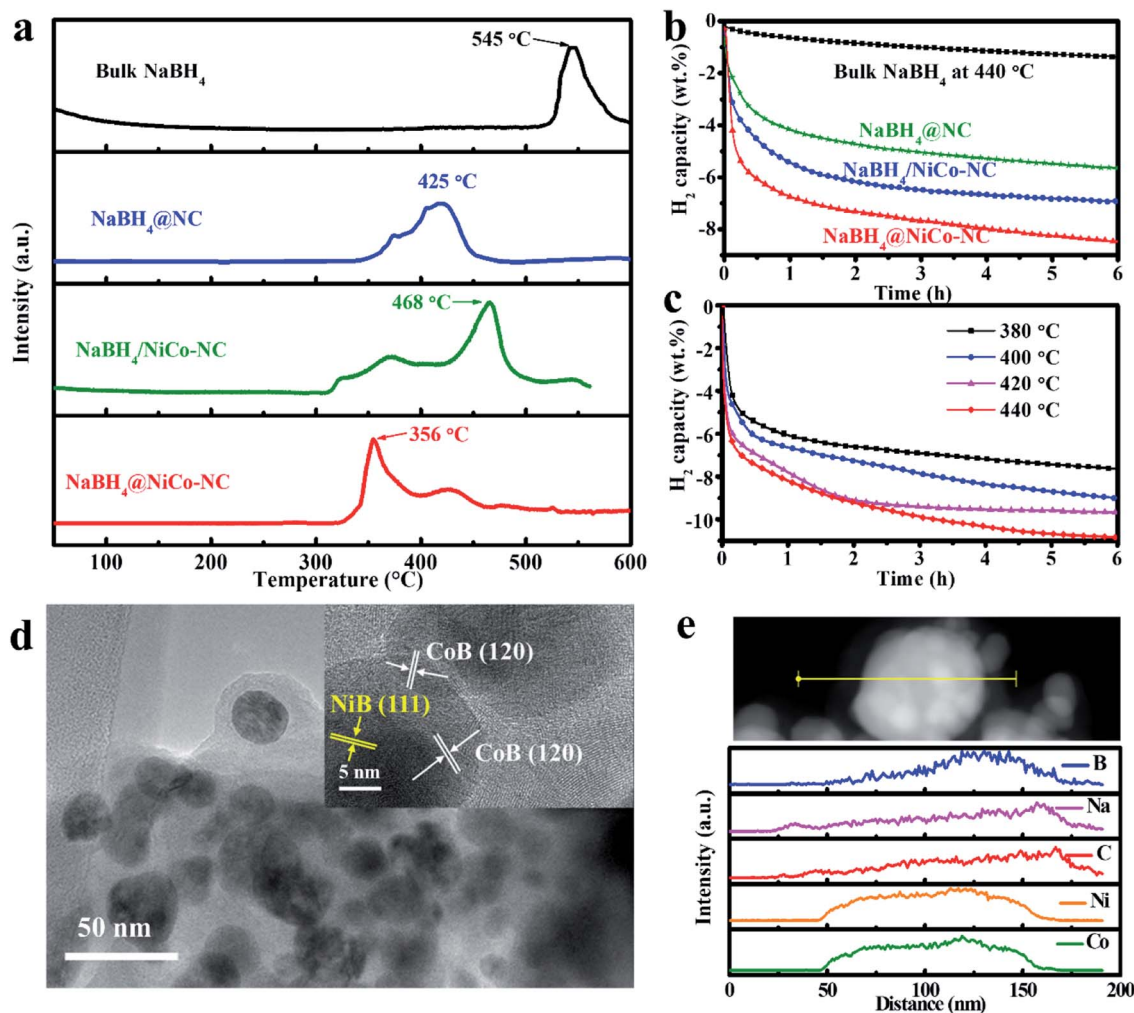
7124 | J. Mater. Chem. A, 2022, 10, 7122–7129

This journal is © The Royal Society of Chemistry 2022

Fig. 2 (a) Mass spectra and (b) the isothermal dehydrogenation kinetics at 380 °C for NaBH$_4$@NiCo-NC, with NaBH$_4$/NiCo-NC, NaBH$_4$@NC, and bulk NaBH$_4$ included for comparison. (c) The isothermal dehydrogenation kinetics of NaBH$_4$@NiCo-NC at various temperatures. (d) TEM and HRTEM (inset) images of NaBH$_4$@NiCo-NC after the initial dehydrogenation process. (e) TEM image and the corresponding line-scan TEM-EDS elemental distribution curves of NaBH$_4$@NiCo-NC after H$_2$ desorption.

are conducted at various temperatures (Fig. 2c), respectively. When the temperature is increased to 440 °C, NaBH$_4$@NiCo-NC is able to release 8.3 wt% hydrogen in a period of only 1 h and a total amount of 10.8 wt% hydrogen, equal to the theoretical hydrogen capacity of NaBH$_4$, could be released from NaBH$_4$@-NiCo-NC upon increasing the heating time to 6 h. In particular, NaBH$_4$@NiCo-NC is capable of releasing 9.0 wt% of hydrogen at a temperature of 400 °C, 1.3 wt% and 2.6 wt% higher than that of NaBH$_4$/NiCo-NC and NaBH$_4$@NC (Fig. S4†).

The presence of NaBH$_4$ could still be detected by XRD patterns (Fig. S5†) for bulk NaBH$_4$ after dehydrogenation at a temperature higher than 550 °C, suggesting incomplete decomposition of NaBH$_4$, which corresponds well with its H$_2$ desorption performance. By comparison, only the diffraction peaks of CoB and NiB in the XRD results could be clearly detected after the dehydrogenation of NaBH$_4$@NiCo-NC with the complete disappearance of NiCo alloys at a temperature as low as 440 °C. The presence of characteristic peaks of NiB and CoB in the XPS spectrum (Fig. S6a–c†) for the dehydrogenation

products of NaBH$_4$@NiCo-NC provides additional evidence for the transformation of NiCo alloys into CoB and NiB during the H$_2$ desorption of NaBH$_4$. More importantly, characteristic peaks of B–H vibrations of NaBH$_4$ are completely disappeared (Fig. S7†), validating the complete dehydrogenation of NaBH$_4$ in NaBH$_4$@NiCo-NC. Hence, the initial H$_2$ desorption reaction of NaBH$_4$@NiCo-NC is illustrated in the following equation:

$$2NaBH_4 + NiCo \rightarrow 2Na + NiB + CoB + 4H_2 \qquad (1)$$
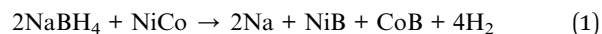
SEM (Fig. S8a†) and TEM (Fig. 2d) images demonstrate that the 2D nanosheet structure of the as-synthesized NaBH$_4$@NiCo-NC is well maintained after the H$_2$ desorption process, with the observation of the uniform distribution of the as-formed NiB and CoB NPs. It is interesting to note that the inner planar spacings of the as-formed nanoparticles revealed by HRTEM images (inset of Fig. 2d) are measured to be 0.22 and 0.20 nm, corresponding to the (120) plane of CoB and (111) plane of NiB, respectively, which agrees well with the XRD (Fig. S5†) and XPS

This journal is © The Royal Society of Chemistry 2022

J. Mater. Chem. A, 2022, **10**, 7122–7129 | **7125**

results (Fig. S6a–c†).[34] TEM-EDS line-scan elemental distribution profiles (Fig. 2e) and EDS elemental mapping images (Fig. S8b†) provide further evidence for the uniform distribution of Na and B from the dehydrogenation products of NaBH$_4$ and C, Co, and Ni from NiCo-NC, indicating the effective space-confinement of NaBH$_4$ into NiCo-NC upon heating for H$_2$ desorption. To quantitatively interpret the nanoconfinement effect of NaBH$_4$ into NiCo-NC in improving its hydrogen desorption kinetics, the apparent activation energies (E_a) for the dehydrogenation of NaBH$_4$ are calculated based on the Arrhenius equation (Fig. S9†). After fitting the experimentally obtained curves at various temperatures, the E_a value of NaBH$_4$@NiCo-NC is calculated to be 36.8 kJ mol^{-1}, much lower than that of both NaBH$_4$@NC (48.9 kJ mol^{-1}) and NaBH$_4$/NiCo-NC (42.5 kJ mol^{-1}). This result provides quantitative evidence for the significantly enhanced H$_2$ desorption kinetics of NaBH$_4$ induced by the synergetic effect of catalysis and nanoconfinement role of NiCo-NC.

Although the reversible stability is a crucial parameter for the practical application of hydrogen storage materials, the cycling hydrogen storage life of NaBH$_4$ is significantly limited due to the phase separation and aggregation of Na, NaH, and B and more importantly, the evaporation of Na upon dehydrogenation, leads to a tremendous loss of reversibility.[17,20] As a result, the atomic ratio between Na and B is detected to be 0.4 after the release of 9.0 wt% hydrogen from bulk NaBH$_4$ at 550 °C (Fig. S10†), resulting in a significant decrease of reversible capacity to 2.5 wt% for the 2nd cycle and 1.8 wt% for the 3rd cycle (Fig. S11†), respectively. Induced by the catalytic effect of NiCo-NC, 7.3 wt% hydrogen could be initially released from the ball-milled composite of NaBH$_4$ and NiCo-NC within a time period of 6 h at 400 °C (Fig. S12a†). The reversible capacity, however, is dramatically reduced to 5.7 wt%, corresponding to a capacity retention of only 78%, after the first cycle of the hydrogen storage process owing to the serious aggregation of dehydrogenation products as revealed by the SEM images (Fig. S13a†). Moreover, although the atomic ratio between Na and B is detected to be 1 in the as-prepared NaBH$_4$/NiCo-NC, this value is dramatically decreased to 0.7 after the release of 9.0 wt% from NaBH$_4$/NiCo-NC due to the tremendous evaporation of Na during the hydrogen storage process (Fig. S14a and b†), which contributes to the serious degradation of cycling capacity to a large extent. In strong contrast, a stable reversible hydrogen storage capacity of 9.0 wt% could be achieved for NaBH$_4$@NiCo-NC even after 5 cycles of hydrogenation and dehydrogenation processes under identical conditions (Fig. 3a), corresponding to a capacity retention of approximately 100% (Fig. 3b). Due to the effective space-confinement role of NiCo-NC, the atomic ratio of Na and B in the dehydrogenated products of NaBH$_4$@NiCo-NC is well maintained, which is comparable to its initial value before dehydrogenation (Fig. S14c and d†). Interestingly, NaBH$_4$ nanoconfined into NiCo-NC after etching of NiCo alloys exhibits an initial H$_2$ desorption capacity of 6.4 wt% (Fig. S12b†) and more importantly, a stable reversible hydrogen capacity of 6.2 wt% could be preserved in the subsequent 2 cycles (Fig. 3b). This result confirms the positive role of nanoconfinement in improving the reversibility of

NaBH$_4$, which could be mainly attributed to the fact that the space-confinement of NaBH$_4$ into the NiCo-NC template could physically inhibit the particle growth and aggregation upon cycling hydrogenation and dehydrogenation processes as evidenced by SEM images (Fig. S13b†).

SEM and TEM images (Fig. 3c and d) illustrate that the uniform distribution of the dehydrogenation products could still be observed for NaBH$_4$@NiCo-NC even after 5 cycles without obvious aggregation of active materials, validating the well-preserved structure of nanoconfined NaBH$_4$ in NiCo-NC. The HRTEM image (Fig. 3e) reveals that the inner planar planes of the nanoparticles are determined to be the (111) plane of NiB and (120) plane of CoB. The relative EDS elemental mapping image (Fig. 3f) provides additional evidence for the uniform distribution of NaBH$_4$ inside of NiCo-NC, indicating the effective nanoconfinement role of NiCo-NC during the repeated de-/re-hydrogenation process, which leads to significantly enhanced reversible hydrogen storage performance.

In order to better unravel the mechanism behind the enhancement of cycling stability, the phase transformation in NaBH$_4$@NiCo-NC during the de-/re-hydrogenation process is subsequently investigated. After the rehydrogenation of NaBH$_4$@NiCo-NC at 350 °C, the characteristic peaks of NaBH$_4$ could be clearly observed in the XRD results (Fig. S15†) with the observation of the signature absorption peaks of NaBH$_4$ in FTIR spectra (Fig. S16†), demonstrating the successful regeneration of NaBH$_4$ at a temperature as low as 350 °C. Interestingly, the diffraction peaks of thus-formed CoB and NiB disappear completely in the XRD results (Fig. S15†) of regenerated NaBH$_4$@NiCo-NC, accompanied by the detection of the characteristic peaks of Ni$_2$B and Co$_2$B. The formation of Ni$_2$B and Co$_2$B could be further supported by the XPS spectrum (Fig. S6d and e†), which illustrates two fitting peaks at 852.4 and 869.7 eV in the Ni 2p XPS spectrum, corresponding to the binding energy of Ni$_2$B, and two fitting peaks located at 778.4 and 792.9 eV in the Co 2p XPS spectrum, corresponding to the binding energy of Co$_2$B.[34,35] In addition, two fitting peaks at 189.1 and 189.9 eV in high-resolution B 1s XPS spectra provide additional evidence for the formation of Ni$_2$B and Co$_2$B (Fig. S6f†). The formation of metal oxides and boron oxides could be attributed to the possible oxidation during sample transfer.[36] The HRTEM image (Fig. S17†) exhibits typical lattice spacings of 0.204 nm and 0.196 nm that could be indexed to the (200) plane of NaBH$_4$ and (211) plane of Co$_2$B or Ni$_2$B, corresponding well with the XRD results (Fig. S15†). Interestingly, after the second cycle of the H$_2$ desorption process, the characteristic peaks of Ni$_2$B and Co$_2$B disappear, accompanied by the reappearance of CoB and NiB (Fig. S18†) in the XRD patterns of NaBH$_4$@NiCo-NC. This result directly demonstrates that after the initial H$_2$ desorption process, the reversible hydrogen storage performance of NaBH$_4$@NiCo-NC could be attributed to the chemical reaction between CoB/NiB and Co$_2$B/Ni$_2$B as illustrated in the following equation:

$$2Na + 2CoB + 2NiB + 4H_2 \leftrightarrow 2NaBH_4 + Ni_2B + Co_2B \quad (2)$$
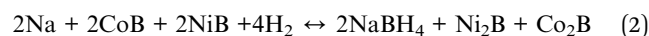
To deeply understand the reversible hydrogen storage performance of NaBH$_4$ improved by NiCo alloys and the *in situ*

7126 | J. Mater. Chem. A, 2022, 10, 7122–7129

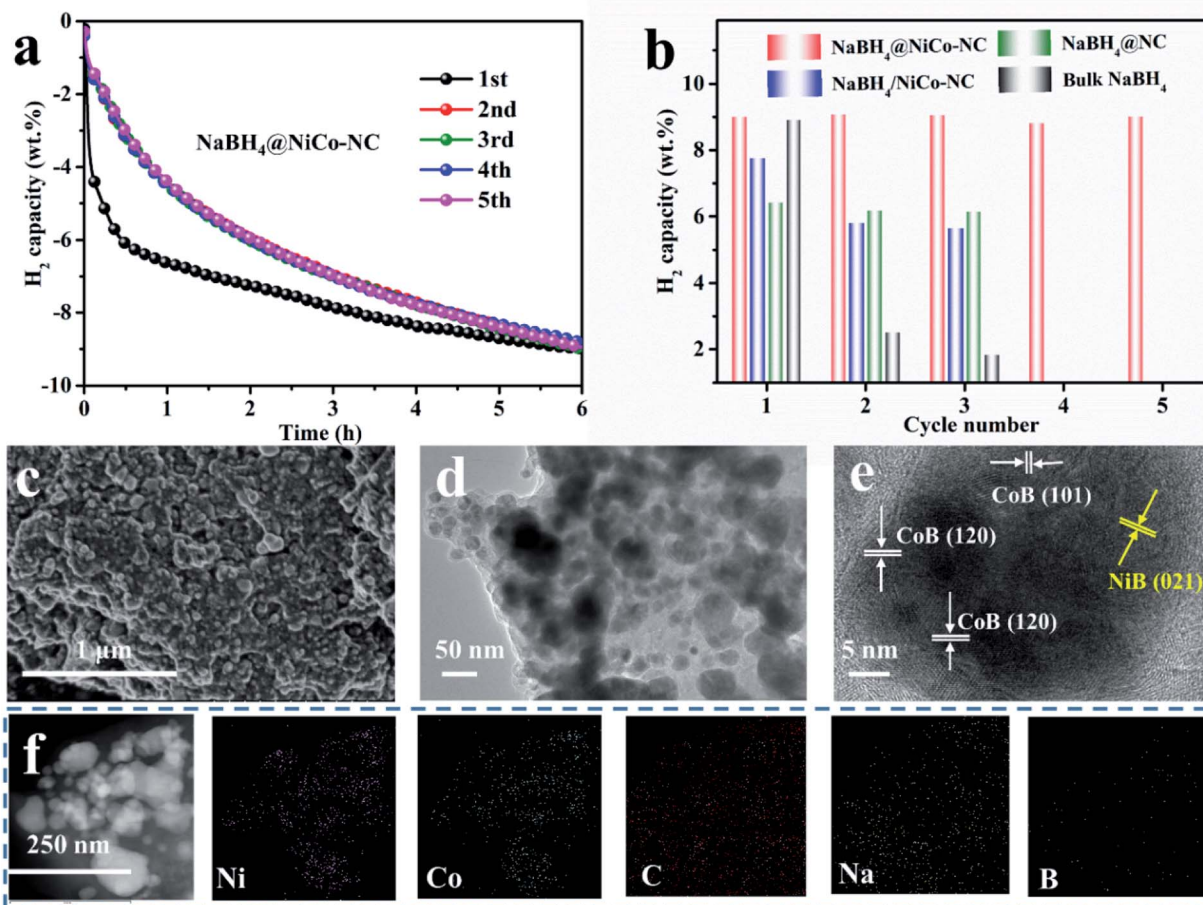This journal is © The Royal Society of Chemistry 2022

Fig. 3 (a) Cyclic H_2 desorption curves of $NaBH_4$@NiCo-NC at 400 °C. (b) Cycling capacity of $NaBH_4$@NiCo-NC, with $NaBH_4$@NC, $NaBH_4$/NiCo-NC, and ball-milled $NaBH_4$ included for comparison. (c) SEM, (d) TEM, (e) HRTEM images and the relative (f) EDS mapping image of $NaBH_4$@NiCo-NC after the 5th dehydrogenation process.

formed metallic borides, phase composition equilibrium calculations based on the Gibbs free energy minimization are conducted. As schematically illustrated in Fig. 4, the equilibrium calculations validate a high Gibbs free energy change of 2.03 eV for the complete reversibility of $NaBH_4$ due to the formation of thermodynamically stable B as the dehydrogenation product. By comparison, upon the interaction with NiCo alloys, the Gibbs free energy change for the decomposition of $NaBH_4$ via the formation of NiB and CoB as the dehydrogenation products according to eqn (1) is decreased significantly to 0.80 eV, indicating the thermodynamically favored reaction between $NaBH_4$ and NiCo alloys towards effectively improved hydrogen desorption performance of $NaBH_4$. More interestingly, during the subsequent rehydrogenation process, the Gibbs free energy change for the reversibility of $NaBH_4$ based on the reversible transformation between NiB/CoB and Ni_2B/Co_2B is decreased to −1.41 eV, much lower than that of eqn (1).

As a result, the subsequent reversibility of $NaBH_4$ would proceed according to eqn (2) without the formation of thermodynamically stable B as the dehydrogenation product. This result directly verifies that the reversible formation of NiB/CoB and Ni_2B/Co_2B could act as a B reservoir to reduce the

thermodynamic stability of the hydrogen storage reaction of $NaBH_4$, which hence thermodynamically improves the hydrogen storage stability of $NaBH_4$. The interaction between Ni_2B/Co_2B and $NaBH_4$ was further calculated to reveal the catalytic mechanism for the catalytic effect of Co_2B/Ni_2B. The average B–H bond length in $NaBH_4$ increased from 1.24 Å to 1.36 Å on Co_2B and 1.31 Å on Ni_2B (Fig. S19†), indicating the capability of both Co_2B and Ni_2B in weakening B–H bonds, which hence promotes the dehydrogenation of $NaBH_4$. In addition, the space-confinement of $NaBH_4$ into NiCo-NC is able to realize homogeneous distribution between $NaBH_4$ and the thus-formed metal borides with intimate contact, which is able to promote the thermodynamically favored reversible transformation between CoB/NiB and Co_2B/Ni_2B. As a result, the hydrogen storage reversibility of $NaBH_4$ could be effectively enhanced. In addition, although the H_2 desorption kinetics of $NaBH_4$@NiCo-NC is slightly deteriorated within the initial 3 h after the first cycle of the dehydrogenation process as shown in Fig. S20,† a comparable reversible capacity of 9.0 wt% could still be obtained in a period of 6 h, much higher than that of the bulk $NaBH_4$ and $NaBH_4$@NC. This demonstrates that the in situ formed Co_2B/Ni_2B still plays a catalytic role in promoting the H_2

This journal is © The Royal Society of Chemistry 2022

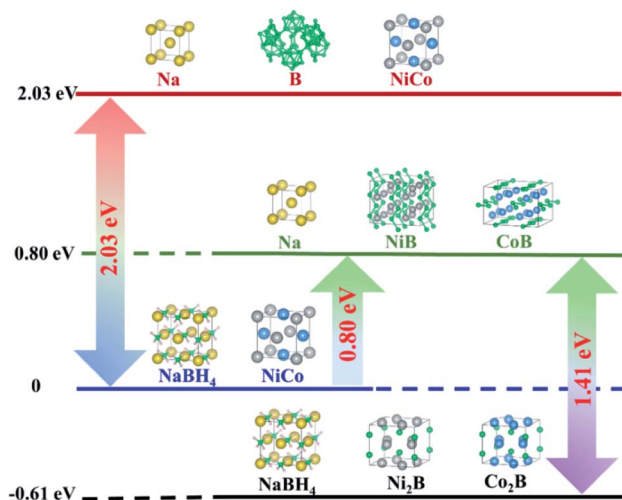J. Mater. Chem. A, 2022, 10, 7122–7129 | 7127

Fig. 4 Thermodynamic calculations for the catalytic mechanism of NiCo NPs in improving the H$_2$ desorption and adsorption processes of NaBH$_4$@NiCo-NC.

desorption performance of NaBH$_4$, while the formation of NiB/CoB as the dehydrogenation products thermodynamically enhances the reversible hydrogenation of NaBH$_4$, which synergistically contributes to improving the cycling stability of NaBH$_4$. In comparison with the nanoconfined NaBH$_4$ as previously reported, the operating temperature, the capacity retention, and the reversible capacity of NaBH$_4$@NiCo-NC are among the best of nanoconfined NaBH$_4$ within various scaffolds (Table S1†).

Conclusions

In this work, we have developed thermodynamically favored reversible hydrogen storage performance of NaBH$_4$ that is *in situ* built inside of bimetallic nanoporous carbon nanosheets. Induced by the synergetic effect of nanoconfinement and catalytic role of NiCo alloys, which thermodynamically and kinetically improves the initial dehydrogenation process of NaBH$_4$ with the formation of NiB and CoB as the dehydrogenation products, the apparent activation energy for H$_2$ desorption from NaBH$_4$ is reduced to 36.8 kJ mol^{-1} with a complete dehydrogenation process at only 440 °C, which is even 83 °C lower than the onset dehydrogenation temperature of bulk NaBH$_4$. More importantly, a thermodynamically favored reversible hydrogen storage process of NaBH$_4$ during the subsequent hydrogen re/de-hydrogenation process is observed based on the reversible transformation between NiB/CoB and Ni$_2$B/Co$_2$B. Taking advantage of the reversible transformation between NiB/CoB and Ni$_2$B/Co$_2$B, which acts as the B reservoir for the reversible dehydrogenation and hydrogenation processes, the Gibbs free energy change for the hydrogen storage of NaBH$_4$ is significantly decreased to 1.41 eV, 0.62 eV lower than that of the bulk counterpart. As a result, coupled with the space-confinement role of NiCo-NC, a stable reversible hydrogen storage capacity of 9.0 wt% is achieved for NaBH$_4$ at 400 °C for five cycles. This finding provides a potential strategy for the design of

a thermodynamically favored hydrogen storage reaction towards practical application.

Conflicts of interest

There are no conflicts to declare.

Acknowledgements

Notes and references

1 T. He, H. J. Cao and P. Chen, *Adv. Mater.*, 2019, **31**, 1902757.
2 M. J. Liu, S. C. Zhao, X. Z. Xiao, M. Chen, C. H. Sun, Z. D. Yao, Z. C. Hu and L. X. Chen, *Nano Energy*, 2019, **61**, 540–549.
3 Q. W. Lai, Y. H. Sun, T. Wang, P. Modi, C. Cazorla, U. B. Demirci, J. R. Ares Fernandez, F. Leardini and K.-F. Aguey-Zinsou, *Adv. Sustainable Syst.*, 2019, **3**, 1900043.
4 L. S. Blankenship Ii, N. Balahmar and R. Mokaya, *Nat. Commun.*, 2017, **8**, 1545.
5 K. Wang, X. Zhang, Y. F. Liu, Z. H. Ren, X. L. Zhang, J. J. Hu, M. X. Gao and H. G. Pan, *Chem. Eng. J.*, 2021, **406**, 126831.
6 Y. R. Wang, X. W. Chen, H. Y. Zhang, G. L. Xia, D. L. Sun and X. B. Yu, *Adv. Mater.*, 2020, **32**, 2002647.
7 S. Wang, M. X. Gao, K. C. Xian, Z. L. Li, Y. Shen, Z. H. Yao, Y. F. Liu and H. G. Pan, *ACS Appl. Energy Mater.*, 2020, **3**, 3928–3938.
8 S.-i. Orimo, Y. Nakamori, J. R. Eliseo, A. Züttel and C. M. Jensen, *Chem. Rev.*, 2007, **107**, 4111–4132.
9 S. Wang, M. X. Gao, Z. H. Yao, Y. S. Liu, M. H. Wu, Z. L. Li, Y. F. Liu, W. P. Sun and H. G. Pan, *Chem. Eng. J.*, 2022, **428**.
10 C. Milanese, T. R. Jensen, B. C. Hauback, C. Pistidda, M. Dornheim, H. Yang, L. Lombardo, A. Zuettel, Y. Filinchuk, P. Ngene, P. E. de Jongh, C. E. Buckley, E. M. Dematteis and M. Baricco, *Int. J. Hydrogen Energy*, 2019, **44**, 7860–7874.
11 P. Martelli, R. Caputo, A. Remhof, P. Mauron, A. Borgschulte and A. Züttel, *J. Phys. Chem. C*, 2010, **114**, 7173–7177.
12 Y. Y. Zhu, L. Z. Ouyang, H. Zhong, J. W. Liu, H. Wang, H. Y. Shao, Z. G. Huang and M. Zhu, *Angew. Chem., Int. Ed.*, 2020, **59**, 8623–8629.
13 L. Z. Ouyang, W. Chen, J. W. Liu, M. Felderhoff, H. Wang and M. Zhu, *Adv. Energy Mater.*, 2017, 7, 1700299.
14 C. J. Tomasso, A. L. Pham, T. M. Mattox and J. J. Urban, *J. Nucl. Energy Sci. Power Gener. Technol.*, 2020, **2**, 1–20.
15 P. K. Singh, I. Sharan, M. Kumar and T. Das, *Int. J. Hydrogen Energy*, 2019, **44**, 20191–20202.

16 T. Wang and K.-F. Aguey-Zinsou, *ACS Appl. Energy Mater.*, 2020, **3**, 9940–9949.

17 L. N. Chong, X. Q. Zeng, W. J. Ding, D. J. Liu and J. X. Zou, *Adv. Mater.*, 2015, **27**, 5070–5074.

18 K. C. Xian, B. Nie, Z. G. Li, M. X. Gao, Z. L. Li, C. X. Shang, Y. F. Liu, Z. X. Guo and H. G. Pan, *Chem. Eng. J.*, 2021, 407.

19 A. Gasnier, G. Amica, J. Juan, H. Troiani and F. C. Gennari, *J. Phys. Chem. C*, 2019, **124**, 115–125.

20 P. Ngene, R. V. D. Berg, M. H. W. Verkuijlen, K. P. de Jong and P. E. de Jongh, *Energy Environ. Sci.*, 2011, **4**, 4108–4115.

21 J. G. Zhang, Y. F. Zhu, H. J. Lin, Y. N. Liu, Y. Zhang, S. Y. Li, Z. L. Ma and L. Q. Li, *Adv. Mater.*, 2017, **29**, 1700760.

22 Q. W. Lai, Y. W. Yang and K.-F. Aguey-Zinsou, *Int. J. Hydrogen Energy*, 2019, **44**, 23225–23238.

23 M. Christian and K.-F. Aguey-Zinsou, *Chem. Commun.*, 2013, **49**, 6794–6796.

24 M. L. Christian and K.-F. Aguey-Zinsou, *ACS Nano*, 2012, **6**, 7739–7751.

25 U. Jeong, H. Kim, S. Ramesh, N. A. Dogan, S. Wongwilawan, S. Kang, J. Park, E. S. Cho and C. T. Yavuz, *Angew. Chem., Int. Ed.*, 2021, **60**, 22478–22486.

26 S. L. Xi, P. Zhang, Y. Y. Fu, K. C. Tome, T. H. Zhang, S. X. Zhou, Y. M. Guo and H. Yu, *Energy Fuels*, 2020, **34**, 10218–10224.

27 C. L. Carr, W. Jayawardana, H. Zou, J. L. White, F. El Gabaly, M. S. Conradi, V. Stavila, M. D. Allendorf and E. H. Majzoub, *Chem. Mater.*, 2018, **30**, 2930–2938.

28 M. S. Salman, A. Rawal and K.-F. Aguey-Zinsou, *Adv. Energy Sustainability Res.*, 2021, **2**, 2100063.

29 I. Llamas Jansa, G. N. Kalantzopoulos, K. Nordholm and B. C. Hauback, *Molecules*, 2020, **25**, 780.

30 Y. Fang, J. Zhang, M. Y. Hua and D. W. Zhou, *J. Mater. Sci.*, 2020, **55**, 1959–1972.

31 S. L. Zhao, Y. Wang, J. C. Dong, C.-T. He, H. J. Yin, P. An, K. Zhao, X. F. Zhang, C. Gao, L. J. Zhang, J. W. Lv, J. X. Wang, J. Q. Zhang, A. M. Khattak, N. A. Khan, Z. X. Wei, J. Zhang, S. Q. Liu, H. J. Zhao and Z. Y. Tang, *Nat. Energy*, 2016, **1**, 16184.

32 S. Q. Zhou, M. Wen, N. Wang, Q. S. Wu, Q. N. Wu and L. Y. Chen, *J. Mater. Chem.*, 2012, **22**, 16858–16864.

33 J. K. Wang, R. Gao, D. Zhou, Z. J. Chen, Z. H. Wu, G. Schumacher, Z. B. Hu and X. F. Liu, *ACS Catal.*, 2017, **7**, 6533–6541.

34 X. Y. Cao, X. X. Wang, L. Cui, D. G. Jiang, Y. W. Zheng and J. Q. Liu, *Chem. Eng. J.*, 2017, **327**, 1085–1092.

35 J. Masa, P. Weide, D. Peeters, I. Sinev, W. Xia, Z. Sun and W. Schuhmann, *Adv. Energy Mater.*, 2016, **6**, 1502313.

36 P. Kukula, V. Gabova, K. Koprivova and K. Trtik, *Catal. Today*, 2007, **121**, 27–38.